Supporting Information

Kiss et al. 10.1073/pnas.1114732109

SI Text

SI Results. ***Crystal contacts.*** As with all crystal structures, crystal contacts may influence the conformation of crystallized proteins. Of the bound MPT, a relatively large part of the exposed surface is devoid of crystal contacts, which are concentrated on the N-and C-terminal regions (Fig. S3). Exceptions from this rule are surface exposed residues of MPT between residues 1912–1915 that interact with subunit A (loop 2). The most intriguing crystal contacts occur between the N-terminal and symmetry related C-terminal part of MPT. As such, the N- and C-terminal helical regions of MPT are in contact (2.7 Å distance between side chains of Asp1902 and Arg1932), and form an almost continuous filament in the crystal structure. This is accompanied by extensive hydrophobic interactions as the C terminus of subunit B wraps around the C terminus of subunit A. Interestingly, the flexible hydrophobic C terminus of S100A4 is bound to the hydrophobic MPT binding cleft in the ligand-free structure of S100A4 between symmetry related molecules (1, 2). A trivial interpretation for the role of C-terminal interactions is that they solely represent fortuitous contacts in the crystalline form. On the other hand, these are more extensive and hydrophobic in nature than typical crystal contacts, and one is tempted to speculate that under certain conditions such interactions may exist in solution, leading to higher order oligomeric structures in which dimeric units either bind individual interaction partners or chain up along a single α-helical peptide containing two or more repeating structural units (Fig. S3).

Symmetry breakage in S100A4 homodimer upon MPT binding. Symmetry breakage is also obvious when we compare the peptide-free, Ca^{2+}-bound wild-type S100A4 (PDB ID code 3C1V) with the mutant protein in complex with MPT by difference distance matrix analysis (Fig. S6). In both subunits, Cα atoms of loop 2 (residues 42–51) are located further away from most part of the dimer in the peptide-bound form. On the other hand, the distance between helix 3 (residues 52–62) and helix 4 (residues 72–92) is shorter in subunit A and longer in subunit B. In this case, the conformation of the peptide-free, Ca^{2+}-bound wild-type S100A4 corresponds to an intermediate position from which the peptide-bound subunits diverge.

Loss of symmetry can also be observed in the atomic displacement parameters (ADPs, expressed in the form of crystallographic B-factors) between the two subunits and the two halves of MPT, respectively. ADPs for subunit A and B are 19.2 ± 9.6 Å^2 and 27.0 ± 13.1 Å^2, respectively. The coupling of the ADPs between the subunits and the bound MPT is apparent when the average ADPs of the N-terminal (residues 1893–1913 interacting with subunit A) and C-terminal (residues 1914–1935 interacting with mainly subunit B) part of the peptide (19.7 ± 9.8 Å^2 and 25.3 ± 12.5 Å^2, respectively) are compared. In contrast, in the Ca^{2+}-bound ligand-free S100A4 dimer (PDB ID code 3C1V) the ADPs are highly symmetric in the four chains that form two dimers in the asymmetric unit (13.9 ± 3.3 Å^2, 13.7 ± 4.2 Å^2, 13.9 ± 3.3 Å^2, and 13.9 ± 4.6 Å^2).

SI Discussion. ***Selective binding of S100A4 to NMII isoforms.*** Among the nonmuscle myosin II isoforms, the most obvious differences in the amino acid sequence can be found in the nonhelical tailpiece that has a major role in subcellular localization of NMII isoforms (3). Moreover, it could also be a component of the selectivity demonstrated by the S100A4-non-muscle myosin II interactions (4). Sequence comparison of MPT in the three isoforms (Fig. 2*A*) reveals a few key interaction residues in NMIIA such as Phe1928 and three residues at the beginning of central helix, that are markedly different in NMIIB. Ala1907 to Asn swap potentially causes steric clash, while the change of Met1910 to Leu affects the tightly packed van der Waals interactions with Val-A77 and Met-A84. Finally, swapping of Asn1911 to Ser may affect the H-bond network displayed on Fig. 3*A*, which may reduce the affinity of NMIIB to S100A4. In the above region MPTc is more similar to MPT, which could explain why S100A4 binds to NMIIC as tightly as to NMIIA (Fig. S1*F*).

SI Methods. ***Expression, synthesis, and purification of proteins and peptides.*** The human wild-type S100A4 (Uniprot code P26447), the NMIIA (P35579), NMIIB (P35580), and NMIIC (Q7Z406) heavy chain fragments were obtained from HEK cell mRNA by reverse transcriptase based PCR. The S100A4 variants, NMIIA MF1 (Ser1712–Glu1960) and MF2 (Gln1795–Lys1937) fragments were cloned after a His_6-tag followed immediately by a Tobacco Etch Virus (TEV) protease cleavage site in the expression vector pBH4 using *Nde*I and *Bam*HI sites. The S100A4 mutants were generated by the megaprimer method (5). Constructs were transformed in BL21-(DE3) Rosetta cells (Novagen). After induction, cells were grown at 37 °C for 3 h in LB medium. His-tagged S100A4 variants were purified on Ni^{2+}-affinity columns (Bio-Rad) in 20 mM Hepes buffer pH 8. To cleave the His_6-tag TEV-protease (6) was added to the eluent and incubated for 3 h at room temperature. The completely digested proteins were applied to a phenyl-Sepharose column (Amersham Biosciences) in the presence of 1 mM $CaCl_2$, washed with 10 column volumes of low ionic-strength buffer and eluted with 5 mM EGTA. After dialyzation to a buffer containing 20 mM Hepes pH 7.5, 20 mM NaCl, and 0.2 mM Tris (2-carboxyethyl)phosphine (TCEP) (Sigma-Aldrich), the protein solutions were concentrated with Amicon Ultra centrifugation filter units (Millipore) to about 5 mM, equimolar amount of TCEP was added and stored in 100 μL aliquots at −70 °C. Note that all the buffers contained 0.2 mM TCEP during the purification of the wild-type proteins to avoid oxidation of reactive thiol groups. The paracrystal forming NMIIA constructs MF1 and MF2 were purified on Ni^{2+}-affinity columns as well. After IMAC purification the N-terminal His_6-tag was cleaved by TEV-protease, and then the protein solution was dialyzed against 20 mM NaCl containing buffer. The pelleted myosin paracrystals were dissolved in 20 mM Hepes pH 7.5, 500 mM NaCl, and 1 mM TCEP, centrifuged for 30 min with 135,000 × *g* in Beckman TL-100 ultracentrifuge (Beckman Coulter), and the supernatant was stored in −70 °C.

The coding DNA of NMII heavy chain peptides MPN (Tyr-Arg1894-Arg1923), MPC (Asp1908-Lys1937), MPT (Tyr-Arg1894-Lys1937), MPTb (Tyr-Arg1901-Arg1944) and MPTc (Tyr-Arg1918-Phe1961) were subcloned to a modified pUBK19 plasmid (7) using *Sac*II and *Bam*HI sites, where *Sac*II site was built in near the 3′ end of the ubiquitin coding sequence. Protein expression and Ni^{2+}-affinity purification were carried out as described previously (7). His-tagged yeast ubiquitin hydrolase (YUH) was added to the eluent while it was dialysed against buffer containing 20 mM Tris pH 8, 100 mM NaCl, and 0.2 mM DTT. His-tagged ubiquitin and YUH were removed by subtractive Ni^{2+}-affinity chromatography. The peptides were finally purified by reverse-phase HPLC on a Jupiter 300 C18 column (Phenomenex). MPC was selectively acetylated on the α-amino groups with a modified method of Wetzel et al. (8). The lyophilized peptide was dissolved in 10 mM MES pH 6, and equimolar glacial acetic acid was added. At this molar ratio, the solution contained

mainly unmodified and α-amino acetylated peptides, which were separated by reverse-phase HPLC as described above. MP0 (Acetyl-Asp1908-Arg1923-$CONH_2$) was synthesized in-house by solid-phase techniques using an ABI 431A peptide synthesizer (Applied Biosystems) and standard *N*-(9-fluorenyl)methoxycarbonyl chemistry. The identity of each peptide and protein was confirmed by mass spectrometry. Concentrations were measured by absorbance at 280 nm using calculated extinction coefficients or by quantitative amino acid analysis.

Circular dichroism (CD) spectroscopy.

$$[\theta]_{222} = \frac{\left(\sqrt{1+\frac{8}{e^{\frac{\Delta H_v}{R}\left(\frac{1}{T_M}-\frac{1}{T}\right)}}}-1\right)\left(e^{\frac{\Delta H_v}{R}\left(\frac{1}{T_M}-\frac{1}{T}\right)}\right)}{4}\left(([\theta]_M + s_{\text{post}}T) - ([\theta]_D + s_{\text{pre}}T)\right) + [\theta]_D + s_{\text{pre}}T, \quad \textbf{[S1]}$$

where $[\theta]_{222}$ is the molar residual ellipticity at 222 nm, ΔH_v is the van't Hoff enthalpy of unfolding, T is the absolute temperature, T_M is the observed melting temperature of the coiled-coil, $[\theta]_M$ and $[\theta]_D$ are the molar residual ellipticities of myosin monomer and dimer, while s_{pre} and s_{post} are the slopes of pre- and posttransitional states, respectively. The statistical uncertainties in T_M and ΔH_v were estimated from the minimum and maximum value of the fixed parameter p for which

$$\text{RSS}(p) < \text{RSS}\left(1+\frac{F}{N-P}\right) \quad \textbf{[S2]}$$

holds. RSS stands for the residual sum of squares differences between the data and the model in Eq. **S1**. RSS and RSS(p) are minimized for all parameters and for all parameters except p, respectively. N denotes the number of data points, and P is the number of parameters. F is the F-distribution value, calculated for alpha level 0.05 and the degrees of freedom 1 and $N-P$. The errors quoted in Table S3 are the average difference between the lower and the upper confidence limit and the parameter value, respectively (9).

Filament disassembly assays.

$$I = I_{\min} + (I_{\max} - I_{\min}) \times \frac{([M]-[S]-K_d+\sqrt{([M]+[S]+K_d)^2-4[S][M]})}{2[M]}, \quad \textbf{[S3]}$$

where K_d is the dissociation constant, $[S]$ is the total concentration of S100A4 dimer, $[M]$ is the total concentration of myosin monomer, I is the measured intensity of light scattering, $I_{\max}$ and $I_{\min}$ are the light intensity values of the solution when the total amount of myosin forms filament or avoids filament formation, respectively.

Crystallization and data collection. Crystallization trials were set up using the sitting drop vapor diffusion method at 20 °C. The drops contained 500 nL of reservoir solution and 500 nL protein-complex solution with 30 mg/mL protein and 7 mg/mL NMIIA fragment (MPT). Crystals grew in reservoir solution containing 30% PEG 4000, 0.2 M Na-acetate pH 5.6, and 0.1 M Na-citrate. Crystals appeared after 2.5 wk and grew to a final size of about 100 μm. A single crystal was flash-cooled in liquid nitrogen using 12.8% glycerol as cryoprotectant. X-ray diffraction data were collected at 100 K with an X-ray wavelength of 0.873 Å on the beamline ID23-2 at the European Synchrotron Radiation Facilities (ESRF, Grenoble, France). In total, 180 frames with an oscillation range of 1° were collected.

Structure determination. High-resolution data for the crystal was processed and scaled in XDS (10) and a molecular replacement solution was found with Phaser (11) using human Ca^{2+}-bound S100A4 (PDB ID code 3C1V) as search model. An initial model was built using Buccaneer/Refmac (12, 13) and flex-wARP (14). Further manual model building was performed in COOT (15), and refinement was carried out in Phenix (16). The final model contained two chains of the S100A4 mutant with 92 amino acid residues (Ala-A2−Pro-A94), and 98 amino acid residues (Met-B1-Arg-B99), respectively, and 2 Ca^{2+} ions in each chain; NMIIA fragment with 43 amino acid residues (Arg1894-Ala1935 plus an N-terminally added Tyr), 2 azide and 2 acetate ions. The overall B-factor of the structure is 24.0 $Å^2$. The structure was validated with Molprobity (17).

Difference distance matrix analysis. An objective comparison of two structures can be performed using difference distance matrices (ddm). Elements in a distance matrix correspond to pairwise internal distances between specific atoms (for example, Cα atoms). A ddm is the difference between two distance matrices provided that the internal distances are measured between equivalent points in the two structures. ESCET (18) calculates and displays ddms while taking into account the coordinate uncertainty of the compared structures. On our ESCET plots, the upper matrix represents the pure distance differences shaded by the magnitude of the difference (in Ångström units) and the lower matrix shows the error weighted difference distances where the distance difference is divided by the error of distance difference (sigma). We estimated the coordinate uncertainty and ultimately the error of distance differences by applying the Cruickshank's DPI-formula (dpiu) (19), which also incorporates individual B-factors in the error estimate. Fig. S2*A* shows the error weighted difference distance matrix between subunit B—subunit A. In Fig. S2*B*, the superposition of subunit A and B is shown based on their structurally invariant regions. ESCET identified 61.3% of all Cα atoms (residues 11–44 and 55–77) as the rigid portion of the structure. We also compared the Ca^{2+}-bound peptide free and MPT bound S100A4 crystal structures using ESCET (Fig. S6). The ESCET plot includes both subunits of the dimer (pairwise distances of Cα atoms in A and B chains of PDB ID code 3C1V minus pairwise distances of equivalent Cα atoms in the A and B chains of PDB ID code 3ZWH). Because the two compared structures are dimers, they have not been superimposed as this would be dominated by the fitting of one subunit.

1. Malashkevich VN, et al. (2008) Structure of Ca^{2+}-bound S100A4 and its interaction with peptides derived from nonmuscle myosin-IIA. *Biochemistry* 47:5111–5126.
2. Gingras AR, et al. (2008) Crystal structure of the Ca^{2+}-form and Ca^{2+}-binding kinetics of metastasis-associated protein, S100A4. *FEBS Lett* 582:1651–1656.
3. Ronen D, Ravid S (2009) Myosin II tailpiece determines its paracrystal structure, filament assembly properties, and cellular localization. *J Biol Chem* 284:24948–24957.
4. Li ZH, Spektor A, Varlamova O, Bresnick AR (2003) Mts1 regulates the assembly of nonmuscle myosin-IIA. *Biochemistry* 42:14258–14266.
5. Sarkar G, Sommer SS (1990) The "megaprimer" method of site-directed mutagenesis. *Biotechniques* 8:404–407.
6. van den Berg S, Lofdahl PA, Hard T, Berglund H (2006) Improved solubility of TEV protease by directed evolution. *J Biotechnol* 121:291–298.
7. Kohno T, Kusunoki H, Sato K, Wakamatsu K (1998) A new general method for the biosynthesis of stable isotope-enriched peptides using a decahistidine-tagged ubiquitin fusion system: an application to the production of mastoparan-X uniformly enriched with 15N and 15N/13C. *J Biomol NMR* 12:109–121.
8. Wetzel R, Halualani R, Stults JT, Quan C (1990) A general method for highly selective cross-linking of unprotected polypeptides via pH-controlled modification of N-terminal alpha-amino groups. *Bioconjug Chem* 1:114–122.
9. Andersson M, et al. (2009) Structural dynamics of light-driven proton pumps. *Structure* 17:1265–1275.

10. Kabsch W (2010) Xds. *Acta Crystallogr D Biol Crystallogr* 66:125–132.
11. McCoy AJ (2007) Solving structures of protein complexes by molecular replacement with Phaser. *Acta Crystallogr D Biol Crystallogr* 63:32–41.
12. Cowtan K (2006) The Buccaneer software for automated model building. 1. Tracing protein chains. *Acta Crystallogr D Biol Crystallogr* 62:1002–1011.
13. Cowtan K (2008) Fitting molecular fragments into electron density. *Acta Crystallogr D Biol Crystallogr* 64:83–89.
14. Cohen SX, et al. (2004) Towards complete validated models in the next generation of ARP/wARP. *Acta Crystallogr D Biol Crystallogr* 60:2222–2229.
15. Emsley P, Cowtan K (2004) Coot: model-building tools for molecular graphics. *Acta Crystallogr D Biol Crystallogr* 60:2126–2132.
16. Adams PD, et al. (2010) PHENIX: a comprehensive Python-based system for macromolecular structure solution. *Acta Crystallogr D Biol Crystallogr* 66:213–221.
17. Chen VB, et al. (2010) MolProbity: all-atom structure validation for macromolecular crystallography. *Acta Crystallogr D Biol Crystallogr* 66:12–21.
18. Schneider TR (2002) A genetic algorithm for the identification of conformationally invariant regions in protein molecules. *Acta Crystallogr D Biol Crystallogr* 58:195–208.
19. Cruickshank DW (1999) Remarks about protein structure precision. *Acta Crystallogr D Biol Crystallogr* 55:583–601.

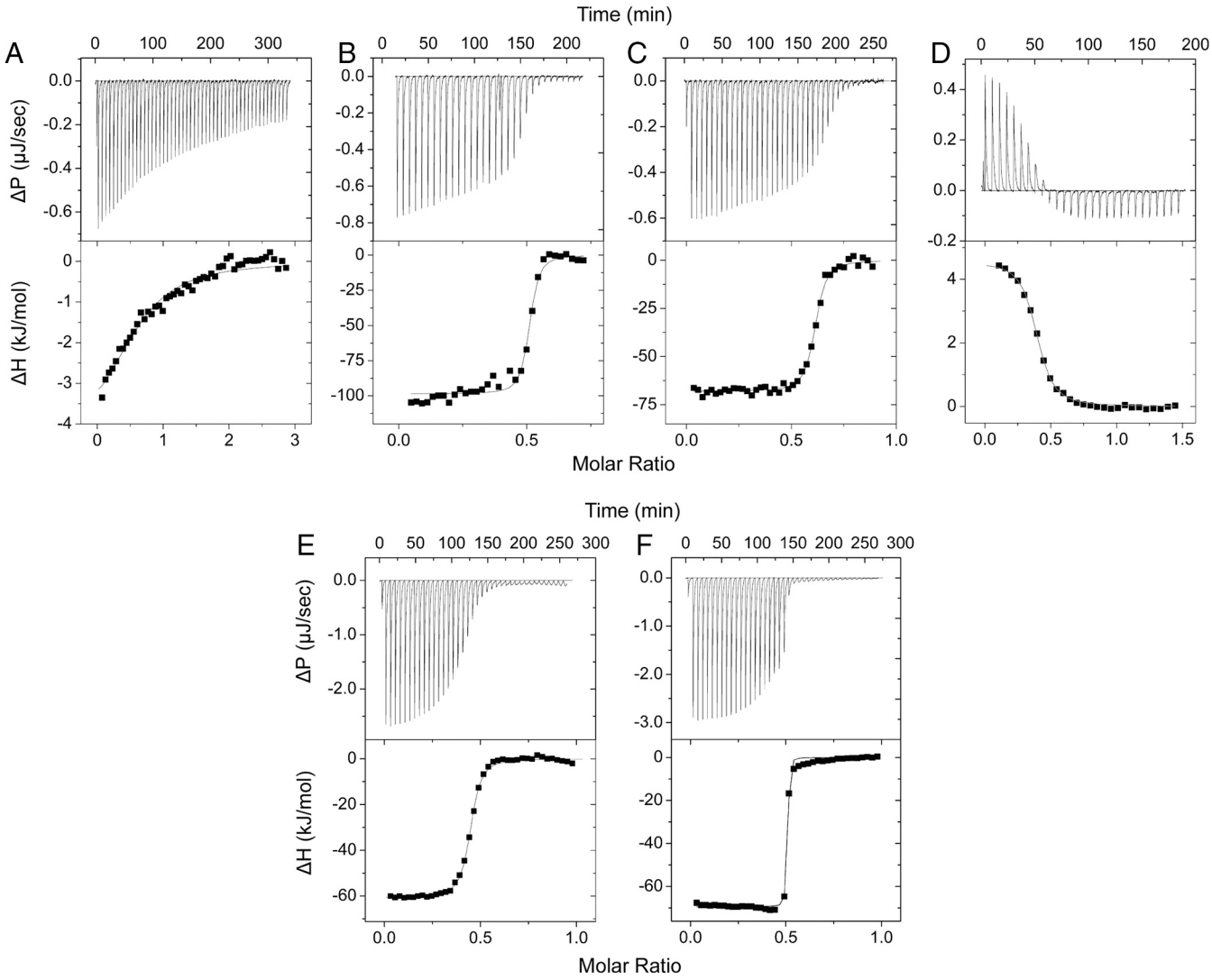

Fig. S1. Affinity of wild-type and mutant S100A4 to NMIIA peptides and fragments. Heat changes were recorded by ITC experiments in conditions described in *Materials and Methods* and Table S2. (*A*) 100 μM wild-type S100A4 was titrated with 1.5 mM MP0. The peptide Asp1908-Arg1923 previously called the "minimal" S100A4-site is a weak-binding partner of S100A4 with $K_d \approx 30$ μM. Interaction of MF2 with wild type (*B*) and S100A4 F45W mutant (*C*) was investigated by titrating 10 μM S100A4 variant with 100 μM myosin fragment. Thermodynamic parameters of the two interactions are similar, indicating that the F45W mutation has only slight effect on myosin binding properties of S100A4. (*D*) 150 μM F45W/C3S/C81S/C86S mutant S100A4 was titrated with 1 mM MPT. Although the binding affinity and the thermodynamic parameters differ from the wild-type S100A4–MPT interaction, the stoichiometry of binding does not change. 75 μM wild-type S100A4 was titrated with 500 μM MPTb (*E*) and MPTc (*F*). The thermodynamic parameters of the interactions are shown in Table S1.

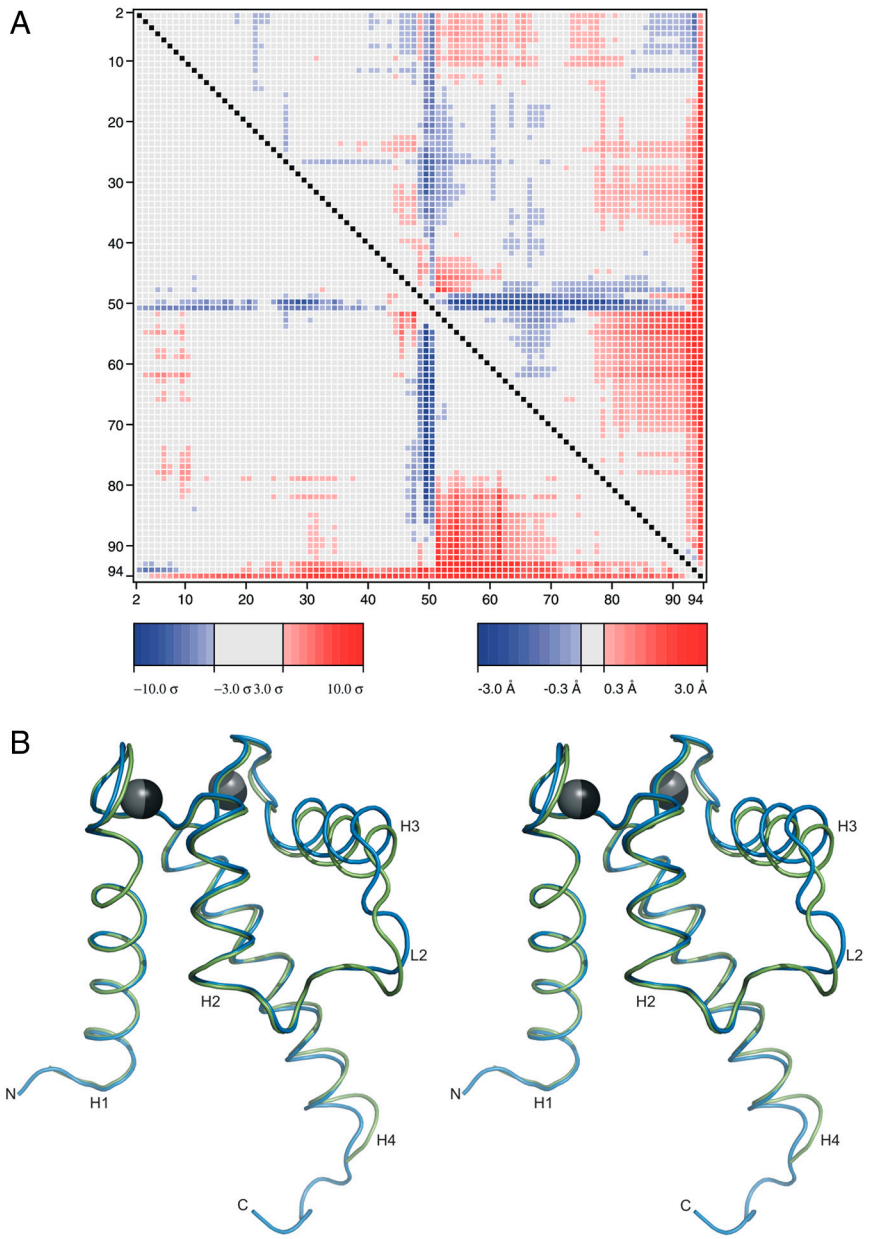

Fig. S2. Structural comparison of subunit A and B in the asymmetric unit. (*A*) Error weighted difference distance matrix (18) between Cα positions (subunit B—subunit A). Blue indicates internal distances shorter in subunit B than in subunit A, whereas red indicates longer internal distances in subunit B. (*B*) Stereo diagram of the least squares superposition of subunit A and B based on the rigid regions of subunit A and B as defined by ESCET (18). Ribbon representation of subunit A is shown in green and subunit B in blue.

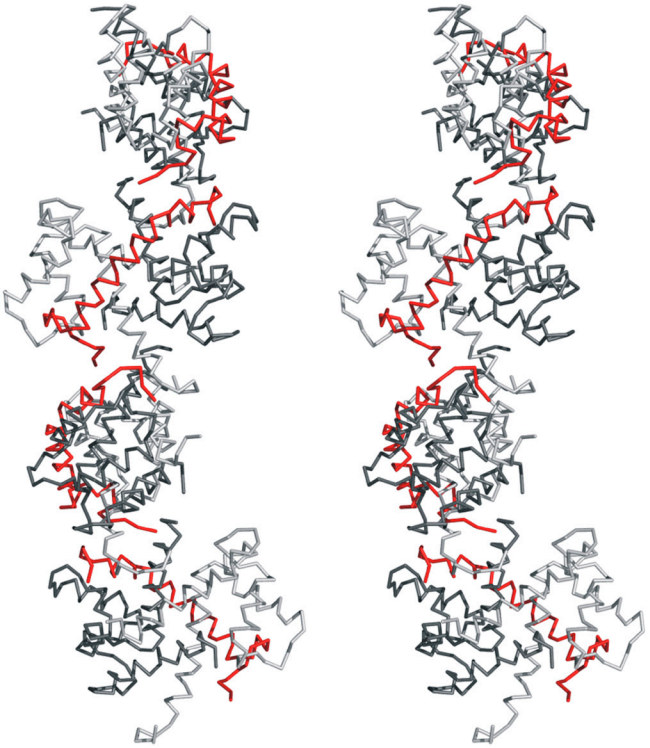

Fig. S3. Stereo diagram of superhelically ordered S100A4–MPT complexes in the crystal-lattice along the crystallographic *c* axis. Ribbon representation of subunit A and B are colored with darker and lighter gray, respectively, while MPT is red. Crystal contacts are seen between the N and C termini of MPT as well as the C-terminal tail of subunit B and a symmetry related subunit A.

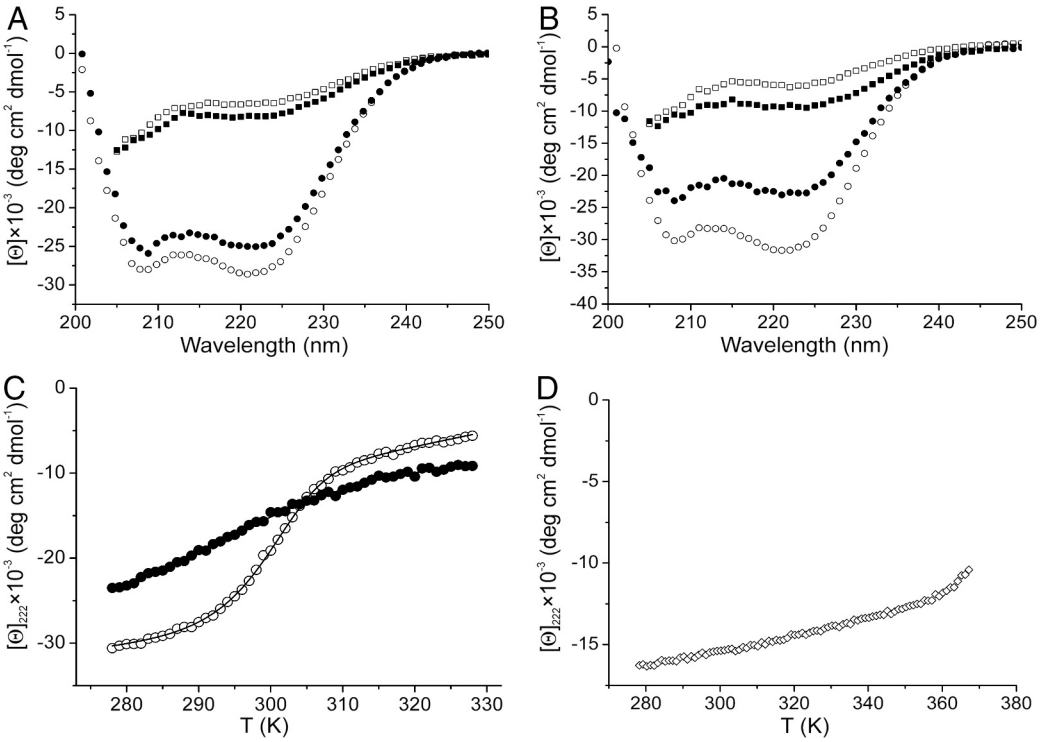

Fig. S4. CD spectroscopic measurements of NMIIA coiled-coil fragments. (*A*) CD spectra of 6 μM MF1 at 15 °C (○) and at 45 °C (□). (*B*) CD spectra of 6 μM MF2 at 5 °C (○) and at 45 °C (□). In *A* and *B*, black symbols show the CD spectra of myosin fragments in the presence of 15 μM S100A4. (*C*) Thermal denaturation profile of free (○) and S100A4-bound (●) MF2. Note that binding of S100A4 decreases the helix content of the coiled-coil; however, the helix content of unfolded state (45 °C) is higher in the complex due to the partial helicalization of S100A4 binding-site (Fig. 5*A*). (*D*) Thermal denaturation profile of S100A4 (15 μM) reveals that at the used experimental conditions S100A4 is highly stable compared to myosin coiled-coil fragments.

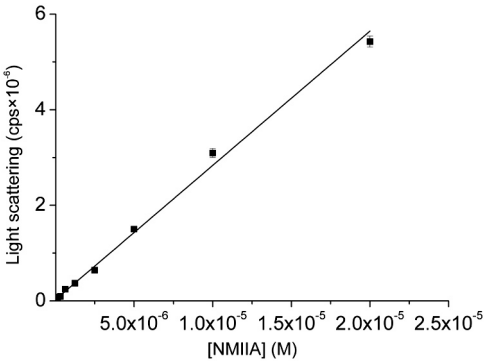

Fig. S5. Light scattering of the MF1 filament. At physiological salt concentration, light scattering is directly proportional to the concentration of the myosin fragment in the observed concentration interval. The data represents the mean ± SEM of three independent measurements.

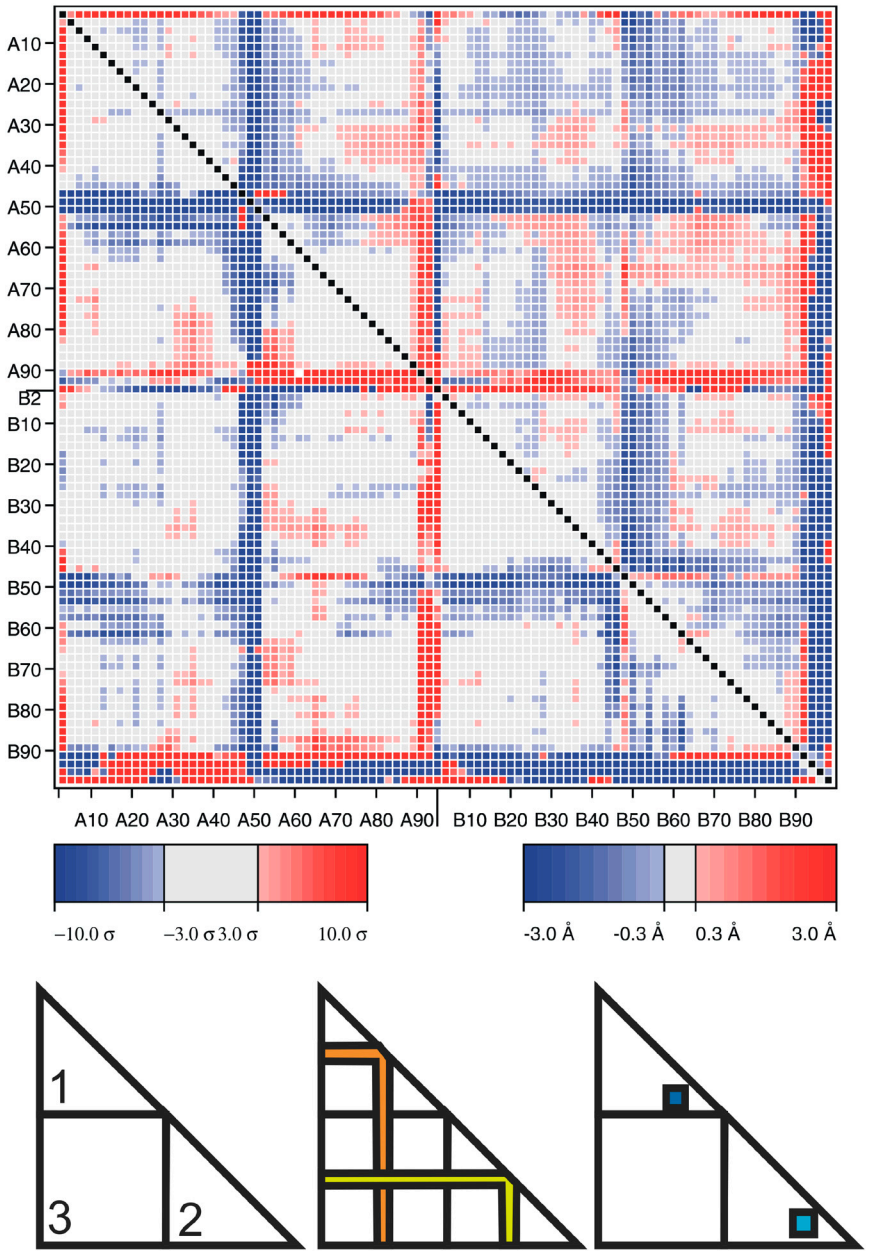

Fig. S6. ESCET comparison between the Ca^{2+}-bound peptide-free and the MPT-bound S100A4 crystal structures (pairwise distances of Cα atoms in A and B chains of PDB ID code 3C1V minus pairwise distances of equivalent Cα atoms in the A and B chains of PDB ID code 3ZWH). Red and blue indicate shorter and longer internal distances in the MPT-bound S100A4 structure, respectively. Coordinate uncertainties were estimated by the Cruickshank's DPI-formula (dpiu)

(19) in ESCET. The schematic diagrams indicate regions describing 1: subunit A-subunit A, 2: subunit B-subunit B 3: intersubunit comparisons in the distance difference matrix. Orange and yellow regions represent the distances between residues 45–55 and the rest of the structure in subunit A and B, respectively. Similarly, blue and cyan indicate the area of the distance difference matrix corresponding to the distances between helix 3 and helix 4 as described in the main text.

Table S1. Thermodynamic parameters of S100A4–NMIIA interactions

Interaction	K_d, nM	ΔH, kJ mol^{-1}	$-T\Delta S$, kJ mol^{-1}
$S100A4_{wt}$ + MP0	27,500 ± 5,390	−4.6 ± 0.5	−21.5
$S100A4_{wt}$ + MPC	1,790 ± 160	−12.6 ± 0.2	−20.3
$S100A4_{wt}$ + MPN	7 ± 1	−98.6 ± 0.3	50.8
$S100A4_{wt}$ + MPT	9 ± 1	−63.2 ± 0.2	17.2
$S100A4_{wt}$ + MPTb	125 ± 9	−60.7 ± 0.3	21.2
$S100A4_{wt}$ + MPTc	2.5 ± 1	−69.4 ± 0.3	20.3
$S100A4_{F45W/C3S/C81S/C86S}$ + MPT	1,540 ± 150	4.8 ± 0.1	−38.0
$S100A4_{wt}$ + MF2	6 ± 2	−98.8 ± 1.2	48.5
$S100A4_{F45W}$ + MF2	11 ± 1	−68.2 ± 0.4	19.4

The affinity of wild-type and mutant S100A4 variants to myosin peptides and fragments MP0, MPN, MPC, MPT was measured in 20 mM Hepes pH 7.5, 150 mM NaCl, 1 mM $CaCl_2$, and 1 mM TCEP at 25 °C. The titration of wild-type S100A4 and F45W mutant with myosin fragment MF2 was carried out in 500 mM NaCl at 47 °C to avoid filament and coiled-coil formation. Stoichiometry of binding in all cases was 0.4–0.6. Note that by affinities in nanomolar range ITC measurements reach the dynamic range limit of the method (18). The values represent the mean ± SEM of the fitted parameters.

Table S2. Crystallographic data and refinement

Data collection	
Space group	$P4_12_12$
Cell dimensions	
$a = b$, c; Å	64.0, 139.0
Resolution, Å*	19.4-1.9 (2.1-1.9)
R_{merge}, %*,†	15.9 (95.3)
$\langle I/\sigma(I)\rangle$*	18.4 (3.5)
Completeness, %*	99.9 (99.7)
Redundancy*	14.3 (15.4)
Refinement	
No. observed reflections	316,617
No. of unique reflections	22,196
R_{work}/R_{free}, %‡	17.5/20.6
No. atoms	
S100A4 chains	1,564
Myosin II fragment	353
Water	201
Total	2,134
B-factors, Å^2	
Chain A, chain B	19.2, 27.0
Myosin II fragment	22.5
Water	31.9
Overall	24.0
Rms deviations from ideal bond parameters	
Bond lengths, Å	0.007
Bond angles, °	0.671
Ramachandran plot§	98.3
Favored, %	
Additional allowed, %	1.7
Outlier, %	0

*Values for the highest resolution shell are shown in parentheses.

†$R_{merge} = \Sigma_h\Sigma_i|I(h)_i - \langle I(h)\rangle I|/\Sigma_h\Sigma_i|I(h)_i|$, where $I(h)_i$ is the ith intensity measurement of reflection and $\langle I(h)\rangle$ is the average intensity from multiple reflections.

‡R-factor $= \Sigma|F_o - F_c|/\Sigma F_o$.

§The percentage of peptide bonds in the most favored and additional region of the Ramachandran plot [determined by MolProbity(3)].

Table S3. Thermodynamic parameters of unfolding of coiled-coil NMIIA fragments

	T_M, K	ΔH_v, kJ mol^{-1}	$K_{d(298K)}$, nM
MF1	308.8 ± 0.1	576.0 ± 10.9	1.8 ± 0.3
S100A4 + MF1	307.0 ± 0.1	444.8 ± 14.0	30.8 ± 5.5
MF2	299.8 ± 0.2	277.2 ± 10.3	3,081 ± 241
S100A4 + MF2*	N.D.	N.D.	N.D.

Apparent melting temperature (T_M) and van't Hoff enthalpy of unfolding (ΔH_v) were determined from the temperature dependence of ellipticity measured at 222 nm assuming a two-state monomer–dimer transition (Eq. **S1**). The values represent the fitted parameters ± their confidence intervals at 95% confidence level. K_d of each myosin fragment (6 μM) at 298 K was calculated from T_M and ΔH_v (19).

*S100A4 binding to the relatively short coiled-coil MF2 considerably decreased the cooperativity of thermal unfolding preventing accurate data analysis (Fig. S4*C*), therefore the thermodynamic parameters were not determined (N.D.).